frontiers | Frontiers in Chemistry

TYPE Original Research
PUBLISHED 05 August 2022
DOI 10.3389/fchem.2022.974907

Check for updates

OPEN ACCESS

EDITED BY
Jianping Sheng,
University of Electronic Science and Technology of China, China

REVIEWED BY
Yuxin Zhang,
Chongqing University, China
Guangming Jiang,
Chongqing Technology and Business University, China

*CORRESPONDENCE
Ying-Zhao Ma,
yzma@cqnu.edu.cn
Wen-Sheng Fu,
fuwensheng@cqnu.edu.cn
Peng Chen,
ctbupengchen@126.com

†These authors have contributed equally to this work and share first authorship

SPECIALTY SECTION
This article was submitted to Catalysis and Photocatalysis, a section of the journal Frontiers in Chemistry

RECEIVED 21 June 2022
ACCEPTED 06 July 2022
PUBLISHED 05 August 2022

CITATION
Zhang W-D, Wang Y, Liang Y, Jiang A-L, Gong H, Tian X-Y, Fu W-S, Liao J-Z, Chen P and Ma Y-Z (2022), High selectivity of photocatalytic reduction of CO_2 to CO based on terpyridine ligand supported Cu^I metal organic framework.
Front. Chem. 10:974907.
doi: 10.3389/fchem.2022.974907

COPYRIGHT
© 2022 Zhang, Wang, Liang, Jiang, Gong, Tian, Fu, Liao, Chen and Ma. This is an open-access article distributed under the terms of the Creative Commons Attribution License (CC BY). The use, distribution or reproduction in other forums is permitted, provided the original author(s) and the copyright owner(s) are credited and that the original publication in this journal is cited, in accordance with accepted academic practice. No use, distribution or reproduction is permitted which does not comply with these terms.

High selectivity of photocatalytic reduction of CO_2 to CO based on terpyridine ligand supported Cu^I metal organic framework

Wen-Dong Zhang[1], Yun Wang[2†], Yi Liang[2†], Ai-Lin Jiang[2†], Hao Gong[1], Xiao-Ying Tian[1], Wen-Sheng Fu[1*], Jia-Zhen Liao[3], Peng Chen[2*] and Ying-Zhao Ma[1*]

[1]Chongqing Key Laboratory of Green Synthesis and Application, College of Chemistry, Chongqing Normal University, Chongqing, China, [2]Chongqing Key Laboratory of Inorganic Functional Materials, College of Chemistry, Chongqing Normal University, Chongqing, China, [3]Chongqing College of Electronic Engineering, Chongqing, China

In this work, a 4′-(4-cynaophenyl)-4,2′:6′,4-terpyridine supported Cu^I MOFs photocatalyst (**Cu^I MOF**) was applied to the photocatalytic CO_2 reduction for the first time. The micro-structural and physicochemical properties of the **Cu^I MOF** were systematically studied by the powder X-ray diffraction (PXRD), Single crystal X-ray diffraction (SCXRD), scanning electron microscope (SEM), X-ray photoelectron spectroscopy (XPS), Fourier transform infrared (FT-IR), UV-Vis diffuse spectroscopy (UV-vis DRS), ns-level photoluminescence spectra (ns-level PL), Ultraviolet photoelectron spectroscopy (UPS), and N_2 adsorption-desorption test (BET-BJH). Moreover, the *in situ* diffuse reflectance infrared fourier transform spectroscopy (*in situ* DRIFTS) was applied to investigate the adsorption and reaction intermediates of photocatalytic CO_2 reduction. As a result, **Cu^I MOF** exhibited good performance and outstanding selectivity toward photocatalytic reduction of CO_2 to CO under full-spectrum and visible light illumination. Notably, 100% selective photocatalytic conversion of CO_2 to CO was achieved. Thus, the study presents the high selectivity and CO_2 reduction efficiency of **Cu^I MOF** as a potential family of photocatalysts.

KEYWORDS

photocatalytic CO_2 reduction, high selectivity, terpyridine ligand, Cu^I MOF, photocatalyst

Introduction

Photocatalytic CO_2 reduction has been regarded as an especially promising approach in light of generating valuable chemical fuels to confront the waste gas CO_2 issues (Chen et al., 2021; Jamjoum et al., 2021). Moreover, owing to its advantages such as the simplicity of utilization, good reusability, low cost, high efficiency and environmental friendliness, various photocatalysts have been designed and applied in photocatalytic CO_2 reduction (Xuan et al., 2020). However, a large amount of photocatalysts still suffers from poor light absorption capacity, high recombination of photo-generated carriers and low selectivity of

product, which limits their practical applications in photocatalytic CO_2 reduction (Fu et al., 2019). Especially, selectivity of product plays the key role during photocatalytic CO_2 reduction. As we all known, photocatalytic CO_2 reduction involves a multi-electron reaction to generate a wide variety of products, including CO, CH_4, CH_3OH and HCOOH, etc., as well as even higher hydrocarbons (Li et al., 2019; Abbas and Sial, 2021) as carbon is in its highest oxidation state. Therefore, catalytic challenge is the precise tuning of the electron density to cater high selectivity. Attempts have been focused on the production of redox photosensitizers to transfer the excited electrons for the catalytic reduction of CO_2. Although the first row transition metal, namely Fe, Co and Ni complexes (Cárdenas-Arenas et al., 2020; Zha et al., 2020; Liu et al., 2021), have been adopted to the substitution of low abundance metal analogues (such as Ru, Re, Os and Ir) (Deng et al., 2018; Deng et al., 2021; Karmakar et al., 2021) as multi-electron catalysts, their quick deactivation excited states (owing to the low lying d-d excited state) has limited the catalytic performance of the CO_2 reduction. Very recently, the heteroleptic Cu^I coordination compounds has gained more attention due to their long lifetimes, showing strong metal-to-ligand (MLCT) excited state emission even in a solution at room temperature dominated by the Cu^I center's d^{10} configuration nature (Yamazaki et al., 2019). Thus, the fine tuning of electron density around the metal center is of great significance. The photophysics and photochemistry of remote substituent effects in coordination compounds have been explored in the past by many groups (Fernández-Terán and Sévery, 2021a). Among them, Fernández-Terán and coworkers adopted 4'-(4-substituted-phenyl)-terpyridine bearing substituents of different electrondonating abilities allowed the remote control of the electron density on the ligands. As the result, the readily tuning of ground- and excited-state properties of the resulting coordination compounds shows the potential of the terpyridine frameworks for high activity/selectivity of photocatalytic reduction chemistry (Fernández-Terán and Sévery, 2021b).

Meanwhile, metal-organic frameworks (MOFs) often possess high thermal and chemical stabilities and allow the incorporation of desired organic ligands featuring various electron-donating abilities through self-assembly and have been gradually applied in the field of catalysis (Zhang and Lin, 2014). Among the reported examples, Cu-based MOFs are highly concerned for its low-price and abundance in nature. In addition, Cu-MOF-based materials have gained extensive attentions as MOF-based catalysts for photocatalytic CO_2 reduction. Wang et al. (Wang X.-K. et al., 2019). Reported that $[Cu_3(TCA)_2\ (dpe)_3(H_2O)_3]_n$ material for photocatalytic CO_2 reduction with the mixture products being CO and H_2. Although the material exhibited good CO_2 reduction activity (CO yield: 68.0 μmol $g^{-1}{\cdot}h^{-1}$), the CO selectivity was merely 22.6%. He et al. (He and Wang, 2018). Fabricated $Cu_3(BTC)_2$-based photocatalysts which can efficiently reduce CO to a mixture of CO and CH_4 (preferential product). Wang et al. (Wang L. et al., 2019). Synthesized PCN-224(Cu) for the photocatalytic reduction of CO_2 under liquid-solid system, which possessed good light harvesting ability. The main reduction products of PCN-224(Cu) were CH_4 and CO. However, although these Cu-MOF-based catalysts exhibited high CO_2 reduction activity, the selectivity was poor. Therefore, it is highly desirable to further regulate Cu MOF catalysts to meet the high selectivity. While, similar to traditional heterogeneous and homogeneous catalysts, the reported Cu^I-MOFs catalysts supported by non-terpyridine ligands also suffer from low CO_2 photocatalytic activity/selectivity. This evokes us to study the photocatalytic CO_2 reduction activity and selectivity of Cu^I-MOFs supported by terpyridine ligands given the aforementioned high activity/selectivity potential of photocatalytic reduction. Thus, the 4'-(4-cynaophenyl)-4,2':6′,4-terpyridine (**L**) supported Cu^I metal-organic-framework (**Cu^I MOF**) reported by Hu and coworkers in 2005 is a good candidate in which **L** features a V-shaped large π-conjugated nonlinear structure. In addition, the cyano group in **L** could be substituted by different electron donating ability groups, allowing the remote control of the electron density to cater the high selectivity of multiple CO_2 reduction products (Xi et al., 2015).

In this work, we adopted **Cu^I MOF** as photocatalyst and its photocatalytic CO_2 reduction activity and selectivity have been studied. It is notable that the **Cu^I MOF** photocatalyst achieved 100% selcetive conversion of CO_2 to CO. Furthermore, UV-vis DRS results indicated that **Cu^I MOF** possesses good light absorption ability (200–800 nm). According to UPS and BET-BJH of **Cu^I MOF**, suitable reduction potential position and high specific surface areas contributed to the high activity of the photocatalytic CO_2 reduction. Finally, *in situ* DRIFT spectra revealed the possible mechanism of photocatalytic CO_2 reduction of **Cu^I MOF**. The synthesis of the **Cu^I MOF** was modified and optimized to allow the delivery of smaller size of the crystalline material. This work not only demonstrated the outstanding photocatalytic CO_2 reduction activity/selectivity of the terpyridine ligand supported Cu^I heteroleptic coordination compounds but also provide a promising strategy for potentially tuning of photocatalytic CO_2 reduction selectivity product based on the ligand substituent group induced rich-electrondonating-diversity featuring terpyridine ligand supported Cu^I-MOFs.

Experimental section

Materials

N,N-dimethylacetamide (DMA), ethanol, potassium hydroxide (KOH), ammonia solution and methanol were purchased from Chengdu kelong chemical Co., Ltd.

Copper cyanide (CuCN), 4-acetylpyridine and 4-formylbenzonitrile were purchased from Shanghai macklin biochemical Co., Ltd. All reagents were directly used as received without further purification.

Synthesis of L

Terpyridine ligand **L** was synthesized according to the literature method (Xi et al., 2015).

Synthesis of Cu^{I} MOF

In a schlenk flask, the mixture of CuCN (1 mmol, 0.09 g), L (2 mmol, 0.70 g) and DMA (20 ml) was stirred under reflux for 12 h. Subsequently, the yellowish green suspension was allowed to cool down to room temperature and washed with DMA (2 × 20 ml), ethanol (2 × 20 ml) and deionized water (2 × 20 ml), in order, by centrifugation. Finally, the product was dried at 80 °C for 12 h (Yield: 0.54g, 67.9%). Anal. Calcd for $C_{108}H_{63}Cu_9N_{27}$ (%): C, 56.09; H, 2.73; N, 16.36. Found: C, 56.43; H, 2.89; N, 16.41.

Activation of Cu^{I} MOF

The as-obtained Cu^{I} MOF sample needed be further activated (3 steps). Step 1: 0.30 g of Cu^{I} MOF was dispersed in 30 ml of DMA with 1 h stirring. Then, the suspension was transferred into a 50 ml Teflon-lined autoclave and heated to 80 °C for 24 h. Step 2: After the Cu^{I} MOF sample cooled down, the obtained catalyst was collected by centrifugation and activated again with ethanol. The activated steps were similar with Step 1, except that conditions was heated to 70 °C for 12 h. Step 3: After the sample cooled to room temperature, the obtained Cu^{I} MOF was collected by centrifugation and washed by ethanol (3 × 20 ml) and deionized water (3 × 20 ml). Next, the sample was dispersed with 5 ml of deionized water and frozen by liquid nitrogen. Finally, the sample was freeze-dried for 24 h.

Characterization and analytical methods

The phase structure of sample was investigated by powder X-ray diffraction (PXRD: model D/max RA, Rigaku Co., Japan). Single crystal X-ray diffraction (SCXRD: Rigaku Oxford Diffraction, Rigaku Co., Japan) was applied to analyze single crystal structure. The morphology and micro-structure were studied with a scanning electron microscope (SEM: JEOL model JSM-6490, Japan). Fourier transform infrared (FT-IR) spectroscopy were implemented by the PerkinElmer Spectrum Two (U.K.), using KBr pellet and analyzing from 400 to 4,000 cm^{-1}. The quantum efficiency and charge carrier lifetime of Cu^{I} MOF were conducted by a fluorescent spectrophotometer (FLS1000, Edinburgh Instruments, U.K.) with 450 nm of excited wavelength. The UV-Vis diffuse spectroscopy (UV-vis DRS: UV2550PC, Shimadzu, Japan) was used to characterize the optical properties. Ultraviolet photoelectron spectroscopy (UPS) measurements (Thermo Fisher Scientific) were carried out on valence band with using a He I ($h\nu$ = 21.2 eV) source. The surface chemical compositions and valence states were analyzed by X-ray photoelectron spectroscopy (XPS) measurements (K-alpha, Thermo Scientific). The specific surface area and pore volume of the sample were measured by the N_2 adsorption-desorption specific surface analyzer (BET, BeiShiDe Instrument, BSD-PS). The elemental analysis for C, H, N were performed on a Perkin-elmer 240C analytical instrument.

Photocatalytic CO_2 reduction

The photocatalytic CO_2 reduction experiment was evaluated using the Labsolar-6A system (Beijing Perfectlight). Before light irradiation, 10 mg of the catalyst was dispersed in 2 ml of pure water, and dropped by droplet onto a fiberglass filter and dried for using. After placing the dried sample in the reactor, the reactor was evacuated until no O_2 or N_2 could be detected via gas chromatography (kechuang, GC 2002). Then, the reactor filled with high-purity CO_2 (≥99.999%, Chongqing lituoqiti Co., Ltd) several times and added 100 μL of deionized water, after which the reaction system pressure in the reactor was maintained at 90.0 ± 1.0 kPa. Then the reactor was exposed to the Xe lamp (lamp current: 20 A, PLS-SXE300+) full-spectrum light illumination for 8 h. The temperature of the entire reaction system was maintained at 20 ± 0.03°C through a recirculating cooling water system. The gaseous products were analyzed every 1 h on the gas chromatograph equipped with a methanizer, flame ionization detector (FID), and thermal conductivity detector (TCD), which could detect CO, CH_4, and H_2, O_2, N_2, respectively.

In situ DRIFTS investigation on photocatalytic CO_2 reduction

In situ DRIFTS measurements (diffuse reflectance infrared Fourier transform spectra) were conducted on a Nicolet iS50FT-IR spectrometer (Thermo Fisher, USA) equipped with a designed reactor and a liquid nitrogen cooled HgCdTe (MCT) detector. Then the loaded samples were purged with Ar (50 $mlmin^{-1}$) for 1 h at 120°C to remove all

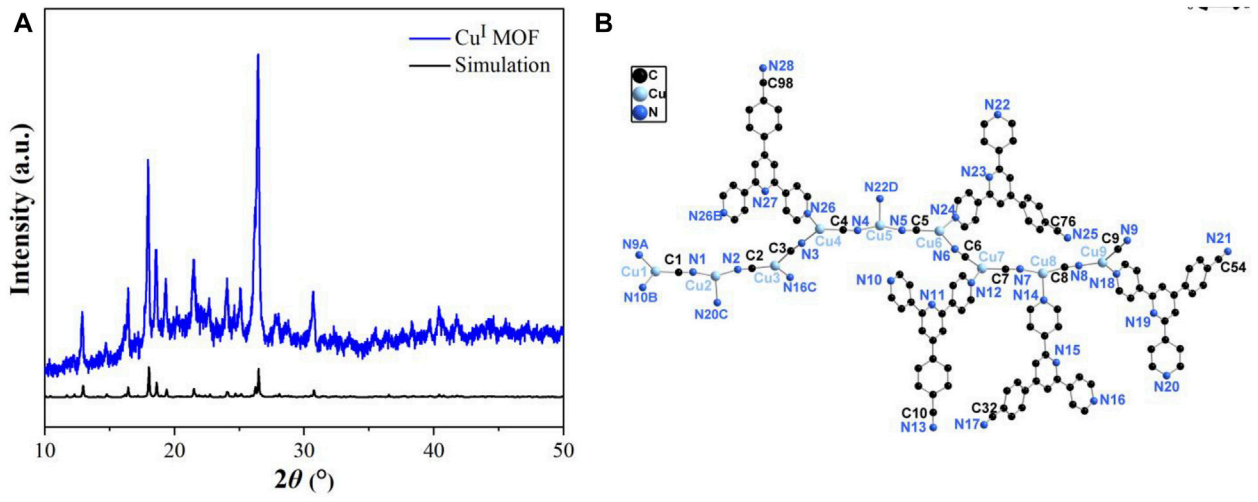

FIGURE 1
(A) Powder XRD pattern and **(B)** view of the coordination environments of **Cu^{I} MOF**.

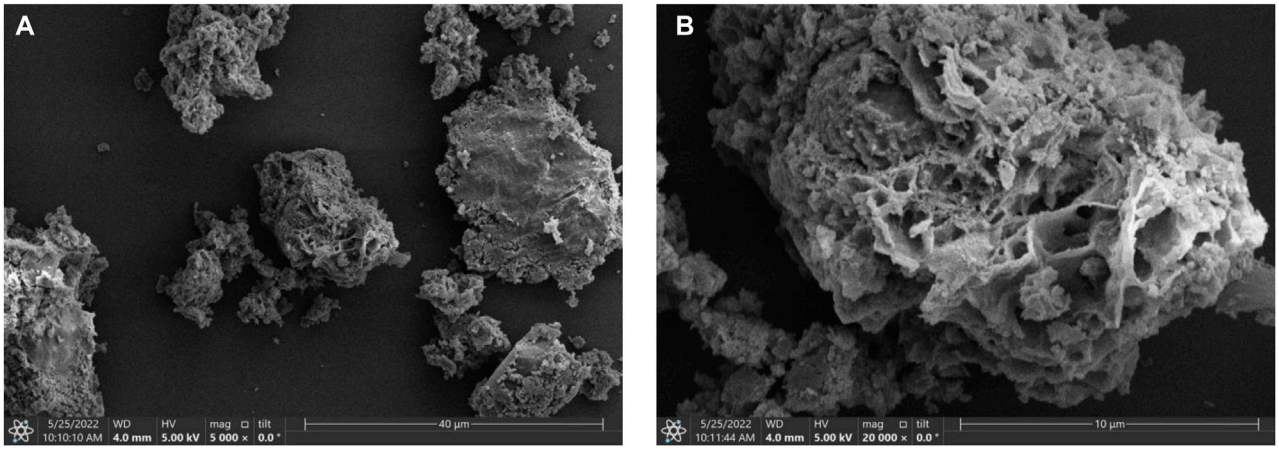

FIGURE 2
SEM images of **Cu^{I} MOF**. Scale bar: 40 μm for **(A)**; 10 μm for **(B)**.

the impurities. After the reactor temperature was dropped to room temperature, the background spectrum was collected. Next, the mixed gas (25 mlmin^{-1} of Ar, 5 mlmin^{-1} of CO_2 and a trace of H_2O vapor) was introduced into the reactor for about 30 min until reaching sorption equilibrium before illumination. Furthermore, the background spectrum was recorded again. Afterward, the turn on the light illumination (300 W Xe Lamp, AM 1.5 G) and the FTIR spectra were recorded as a function of time to investigate the dynamics of the conversion of the reactants under illumination.

Results and discussion

Phase structure

As shown in Figure 1A, the characteristic diffraction peaks can be well matched with single crystal simulation (SIM) patterns, which not only indicating the successful synthesis of **Cu^{I} MOF**, but also conformed the phase purity of it. Notably, the considerably sharp diffraction peaks of **Cu^{I} MOF** reveals the good crystallinity. The structure illustration of **Cu^{I} MOF** was presented in Supplementary

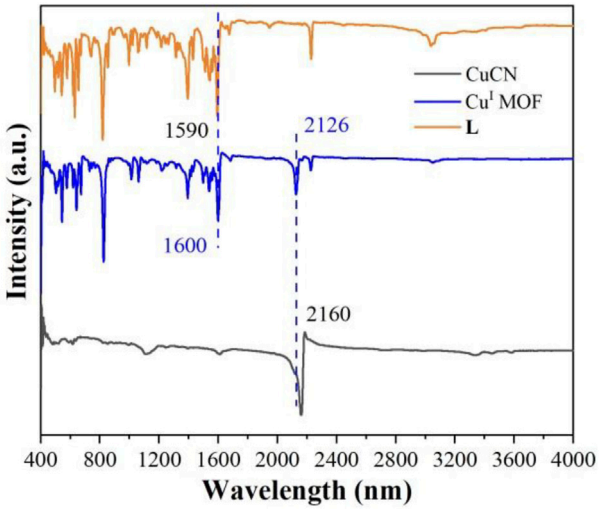

FIGURE 3
FT-IR spectra of **Cu^{I} MOF**.

Figure S1 and Figure 1B. **Cu^{I} MOF** is a three dimensional interpretation structure. The asymmetric unit comprised by nine Cu^{I} ions, four and a half ligands and nine cyanide ions with all the bond lengths and angles are identical to the structure reported (Xi et al., 2015).

Micro-structure and morphology

SEM was carried out to explore the micro-structures and morphologies of the **Cu^{I} MOF**. As depicted in Figure 2A, the as-obtained **Cu^{I} MOF** demonstrates irregular and fluffy porous structure. Figure 2B further confirms that the tremella-like morphology of **Cu^{I} MOF** is self-assembled by plenty of the stacked nanosheets and nanoparticles.

FT-IR spectra

The FT-IR spectra of the as-prepared **Cu^{I} MOF**, CuCN and **L** were illustrated in Figure 3. The significant peaks at 1,590 and 1,600 cm^{-1} were attributed to the C=C/C=N stretching vibration of pyridine (Singh et al., 2021). The band at 2,126 and 2,160 cm^{-1} were ascribed to the C≡N stretching vibration (Zhang et al., 2018). Compared to CuCN (2,160 cm^{-1}) and **L** (1,590 cm^{-1}), the C≡N and C=C/C=N characteristic peaks of **Cu^{I} MOF** shifted, respectively, suggesting that CuCN and **L** are coodinated. Moreover, the existence of CuCN and **L** characteristic peaks of **Cu^{I} MOF** sample indicated that **Cu^{I} MOF** was successfully synthesized by this method.

XPS

The XPS was carried out to investigate the surface chemical compositions and valence states of **Cu^{I} MOF** sample. As can be seen from Figure 4A, the XPS survey spectrum reveals the presence of C, N, O and Cu elements in **Cu^{I} MOF** sample. In the high resolution Cu 2p spectra (Figure 4B), the main peaks at 952.6 and 932.8 eV are assigned to Cu^{I} (Zhu et al., 2021). To further identify Cu^{I}, Cu LMM Auger spectrum as shown in Figure 4F. The Cu Auger LMM peak was observed at 571.9 eV (Jiang et al., 2022) in the binding energy scale, which was corresponded to the characteristic peak of Cu^{I}. These results show that the valance of copper existed as Cu^{I} in **Cu^{I} MOF.** As displayed in Figure 4C, the peaks at 285.7 and 284.8 eV in the high resolution C 1s spectra are ascribed to the C-N and C=C/C-C bond in the **L** (Zhu et al., 2021). The high resolution N 1s spectra of **Cu^{I} MOF** sample is provided in Figure 4D. Binding energy at 399.3 and 398.6 eV are indexed to Cu-N bond (Zhu et al., 2021) and pyridinic N (Singh et al., 2021), respectively. The formation of Cu-N bond proved that the Cu elements were successfully coordinated with the cyano groups and the N in the **L**. The high resolution O 1s spectra is demonstrated in Figure 4E. It can be found that the binding energies at 533.4 and 531.8 eV correspond to O-H bonds of surface absorption water and Cu-O (H_2O) interactions (Liu et al., 2021), respectively.

UV-vis DRS and ns-level PL

The UV-vis diffuse reflectance spectra of **Cu^{I} MOF** have been conducted to evaluate its light absorption ability (Figure 5A). **Cu^{I} MOF** displayed good absorption ability in the ultraviolet and visible region, which is in good consistent with the color of **Cu^{I} MOF** sample (inset of Figure 5A). In Figure 5B, the band gap of **Cu^{I} MOF** has been calculated from the intercept of the tangents to the plots of $(\alpha h\nu)^{1/2}$ vs. Photo energy is 2.36 eV. The time-resolved PL spectra as depicted in the Figure 5C, the carrier lifetime of **Cu^{I} MOF** is 0.08 ns? Furthermore, the quantum efficiency of **Cu^{I} MOF** is 1.32% under visible light (450 nm) illumination.

UPS

UPS was conducted to investigate the position of valence band (VB) and conduction band (CB). The abscissa is the binding energy which is relative to the Fermi energy (E_F) of Au. It is defined by the energy of the electron before excitation relative to the vacuum level. The high binding energy cutoff (E_{cutoff}) of **Cu^{I} MOF** is illustrated in Figure 6A. E_{cutoff} is decided by linear extrapolation to zero of the yield of secondary electrons. In Figure 6A, E_{cutoff} = 16.3 ± 0.03 eV for **Cu^{I} MOF**. The HOMO region for **Cu^{I} MOF** is observed in Figure 6B. The HOMO energy

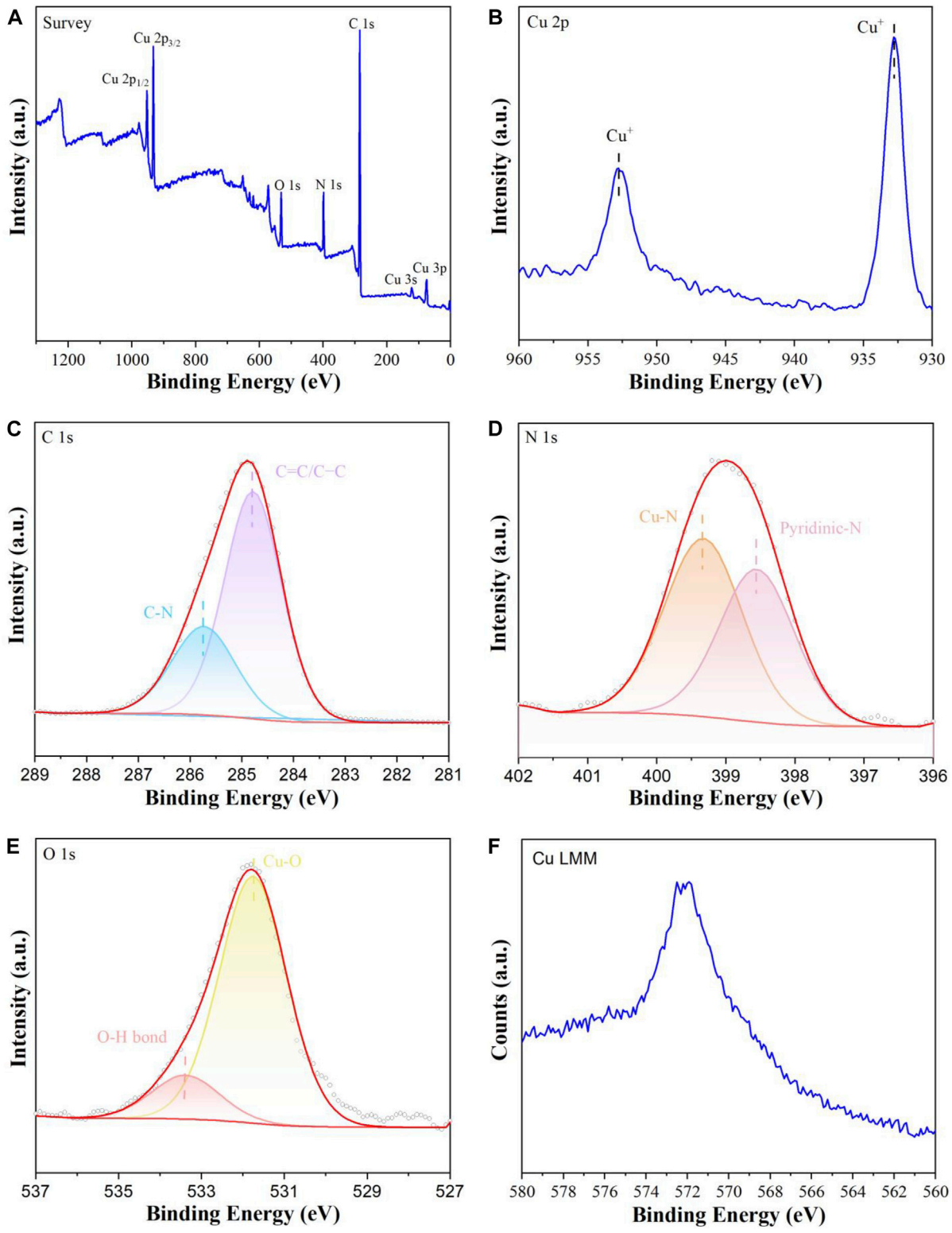

FIGURE 4
(A) XPS survey spectra of **Cu^{I} MOF**, high resolution spectra of **(B)** Cu 3d, **(C)** C 1s, **(D)** N 1s, **(E)** O 1s, **(F)** Cu LMM Auger spectrum for in **Cu^{I} MOF**.

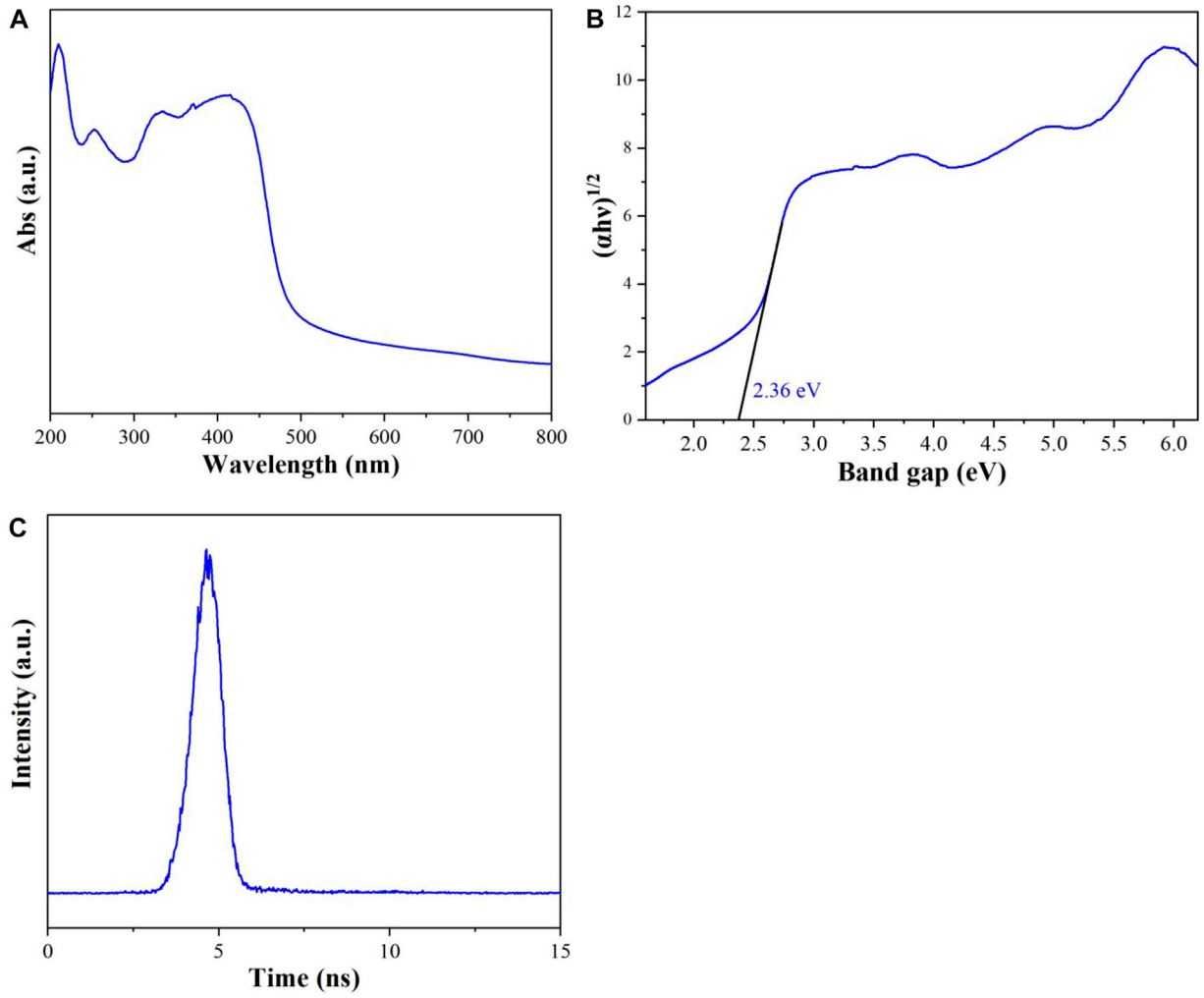

FIGURE 5
(A) UV-vis diffuse reflectance spectra, **(B)** plots of $(\alpha h\nu)^{1/2}$ vs. Photo energy and **(C)** time-resolved PL spectra monitored at under 450 nm excitation at 298 K for **Cu^{I} MOF**.

is decided using the incident photon energy, $h\nu$ = 21.2 eV, E_{cutoff}, and the E_{onset} (the onset of **Cu^{I} MOF** relative to the E_F of Au). In Figure 6B, E_{onset} = 0.98 ± 0.03 eV for **Cu^{I} MOF**. The HOMO energy is thus gained directly from the UPS measurement, $E_{HOMO} = h\nu-(E_{cutoff} - E_{onset})$ (Gong et al., 2011; Sun et al., 2011; Zheng et al., 2018).

For **Cu^{I} MOF**, E_{HOMO} = -5.88 ± 0.06 eV. The LUMO energy is calculated using the HOMO levels and the optical gaps (E_g) obtained from UV-Vis DRS (Figure 5B). Thus, the E_{LUMO} = -3.52 ± 0.06 eV is for **Cu^{I} MOF**. Concequnently, the photo-generated electrons of **Cu^{I} MOF** could reduce CO_2 to CO. According to the characterization results of UPS and UV-vis diffuse reflectance spectra (Figure 5A, Figure 6), the diagram of band structure is shown in Figure S4.

BET-BJH

As can be seen from Figure 7A, the N_2 adsorption-desorption isotherm of **Cu^{I} MOF** exhibits typical IV isotherms with H3 type hysteresis loop, which indicates the existence of mesopores. The pore size distribution curve further demonstrates the existence of mesopores (Figure 7B). The specific surface area, corresponding pore volume and average pore diameter are 116.98 $m^2 g^{-1}$, 0.77 $cm^3 g^{-1}$ and 26.40 nm respectively. The high specific surface area and large pore volume could provide more active sites for the reactant adsorption and photocatalytic reaction, which is in agreement with SEM result.

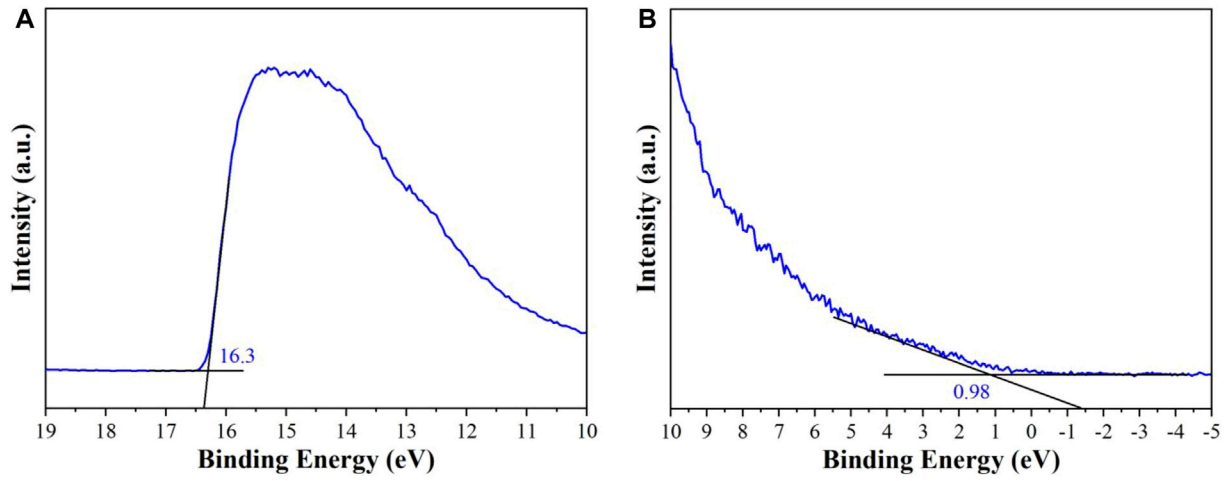

FIGURE 6
(A) The secondary edge region and **(B)** the HOMO region of UPS spectra of **Cu^{I} MOF**.

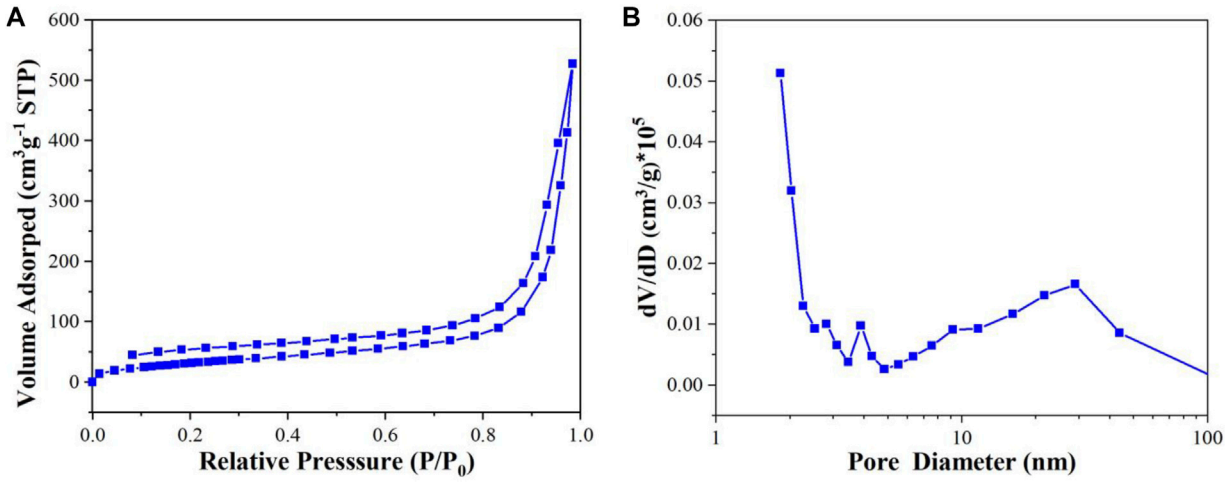

FIGURE 7
(A) N_2 adsorption-desorption isotherm curves and **(B)** pore size distributions of **Cu^{I} MOF**.

Photocatalytic performance

The experiment of full-spectrum light (AM 1.5 G) driven CO_2 reduction was performed to evaluate the photocatalytic activity. Before the beginning of photocatalytic CO_2 reduction, no CO and other organic matter are detected under the reaction conditions of without light, photocatalyst and with Ar atomosphere, respectively, demonstrating that CO_2 is the sole carbon source for the reaction. As shown in Figure 8A, it is interesting that the CO concentration was found to increase gradually with the extension of the illumination time. After 8 h of photocatalytic reaction, no other product can be detected additional to CO, which suggests that the selectivity of CO production is 100%. It is worthwhile mentioning that the yield rate of CO is 2.58 μmol g^{-1}·h^{-1} under 8 h full-spectrum light illumination. Remarkably, **Cu^{I} MOF** also shows a good visible light photocatalytic activity for CO_2 reduction, whose yield rate of CO is 1.83 μmol g^{-1}·h^{-1} under 8 h illumination (Figure 8B). Moreover, the photocatalytic stability of **Cu^{I} MOF** was assessed through three sequent tests of photocatalytic CO_2 reduction for 24 h (Supplementary Figure S2). The yield of CO dropped from about 2.58 to 0.87 μmol g^{-1}·h^{-1}, which suggested poor photocatalytic stability. The poor photocatalytic stability could be due to photo-

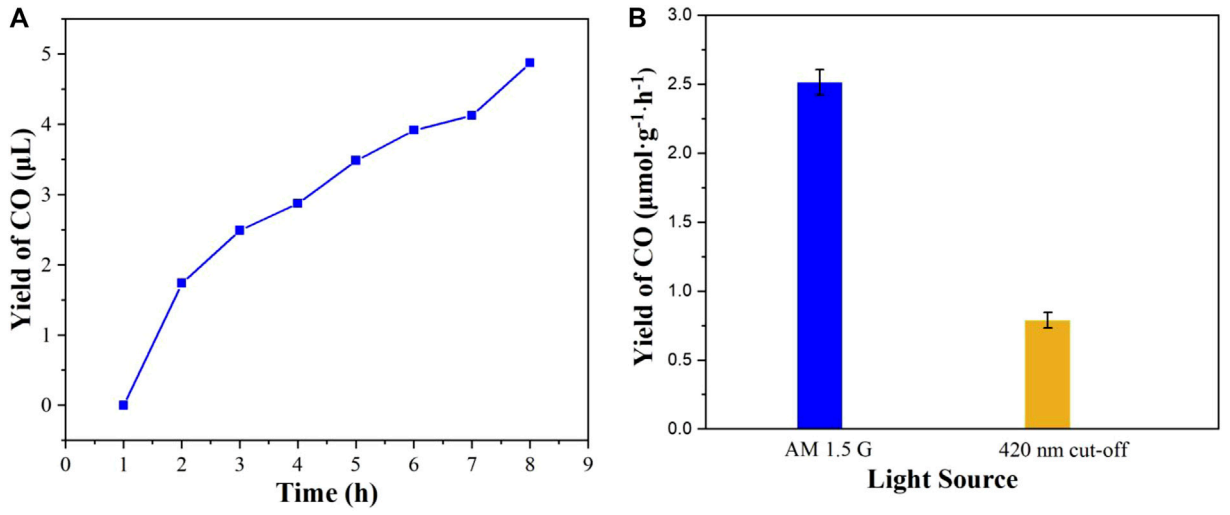

FIGURE 8
(A) The yields of CO reduced by CO_2 under AM 1.5 G illumination and **(B)** the yields rate of CO under different light source illumination.

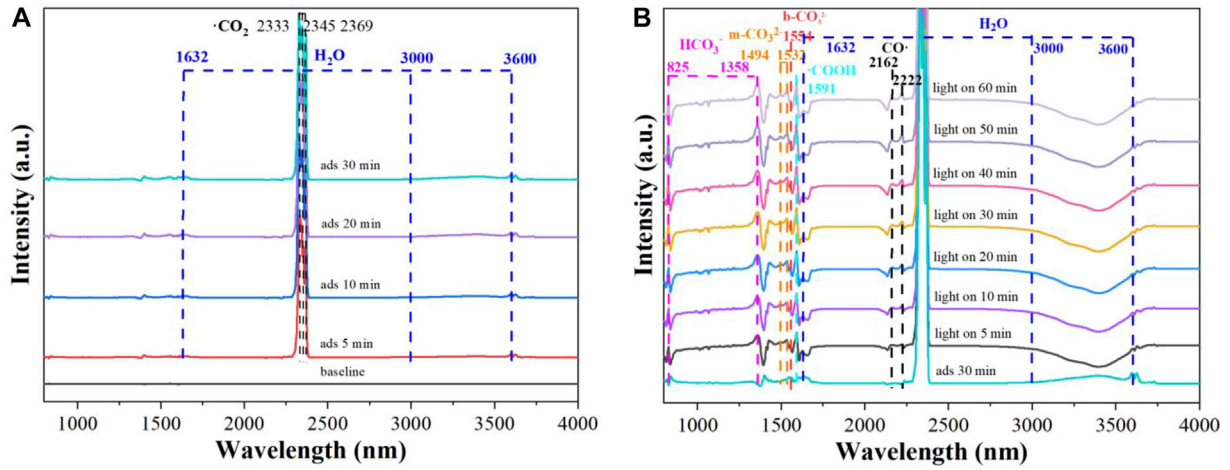

FIGURE 9
(A) *In situ* DRIFT spectra of CO_2 and H_2O absorption and **(B)** reaction on **Cu^I MOF**.

destabilization of functional groups (Feng et al., 2020), which decomposed the framework of **Cu^I MOF** and caused poor photocatalytic stability.

Mechanisms of photocatalytic CO_2 reduction

As can be seen in Figure 9A, the peaks at 2,333, 2,345 and 2,369 cm^{-1} are indexed to CO_2 (Coenen et al., 2018) and the peaks at 1,632 and 3,000–3,600 cm^{-1} are attributed to H_2O (Tang et al., 2019; Zhao Y. et al., 2020), respectively. Furthermore, the intensities of the peaks increase with prolonged absorption time, which indicates that CO_2 molecules are activated on the surface of **Cu^I MOF**.

In Figure 9B, after light turned on, a number of intermediates are detected, including HCO_3^- (825 and 1,358 cm^{-1}) (Liu et al., 2017; Ma et al., 2017), b-CO_3^{2-} (1,554 cm^{-1}) (Tang et al., 2019), m-CO_3^{2-} (1,494 and 1,532 cm^{-1}) (Liu et al., 2017), –COOH (1,591 cm^{-1}) (Zhao J. et al., 2020) and CO (2,162 and 2,222 cm^{-1}) (Ma et al., 2017). Moreover, the intensities of thoes peaks gradually enhanced with the extension of

illumination time. Accordingly, the possible CO_2 conversion pathway was proposed as following:

$$CO_2 + H_2O \rightarrow HCO_3^- + H^+ \quad (1)$$

$$HCO_3^- \rightarrow CO_3^{2-} + H^+ \quad (2)$$

$$CO_2 \uparrow \rightarrow \bullet CO_2 \quad (3)$$

$$\bullet CO_2 + H^+ + e^- \rightarrow \bullet COOH \quad (4)$$

$$\bullet COOH + H^+ + e^- \rightarrow CO\bullet \quad (5)$$

$$CO\bullet \rightarrow CO \uparrow \quad (6)$$

Conclusion

In summary, the synthesis of **Cu^I MOF** was successfully optimized for photocatalytic CO_2 reduction. The CO evolution reached 2.58 μmol $g^{-1}{\cdot}h^{-1}$ and achieved 100% conversion. Moreover, UV-vis DRS result indicates that **Cu^I MOF** displays good light absorption capacity (200–800 nm). The BET-BJH result reveals that **Cu^I MOF** possesses high specific surface area (116.98 $m^2\ g^{-1}$) and large pore volume (0.77 $cm^3\ g^{-1}$). The position of conduction band (-3.52 ± 0.06 eV) of **Cu^I MOF** is negative enough to meet the photocatalytic CO_2 reduction. Finally, the possible mechanisms of photocatalytic CO_2 reduction were revealed by the *in situ* DRIFTS. This study demonstrated the promising potential of terpyridine ligand supported Cu^I-MOFs for the high activity/selectivity of photocatalytic CO_2 reduction.

Data availability statement

The original contributions presented in the study are included in the article/Supplementary Material; further inquiries can be directed to the corresponding authors.

Author contributions

W-DZ and Y-ZM designed the experiments. YW, A-LJ, HG, and X-YT carried out photocatalyst **Cu^I MOF** synthesis. W-SF, J-ZL, and PC worked on the material property data analysis.

Funding

This research is financially supported by the National Natural Science Foundation of China (Grant No. 51708078), Natural Science Foundation of Chongqing (Grant No. cstc2021jcyj-msxm2068) the Science and Technology Research Program of Chongqing Municipal Education Commission (Grant No. KJZD-K201900502), Chongqing Talent Program (Leading Talent), and the Chongqing Innovative Research Group Project (Grant No. CXQT21015, CQYC201903221).

Conflict of interest

The authors declare that the research was conducted in the absence of any commercial or financial relationships that could be construed as a potential conflict of interest.

Publisher's note

All claims expressed in this article are solely those of the authors and do not necessarily represent those of their affiliated organizations, or those of the publisher, the editors and the reviewers. Any product that may be evaluated in this article, or claim that may be made by its manufacturer, is not guaranteed or endorsed by the publisher.

Supplementary material

The Supplementary Material for this article can be found online at: https://www.frontiersin.org/articles/10.3389/fchem.2022.974907/full#supplementary-material

References

Abbas, M., and Sial, M. A. Z. G. (2021). New Horizon in stabilization of single atoms on metal-oxide supports for CO2 reduction. *Nano Mater. Sci.* 3, 368–389. doi:10.1016/j.nanoms.2021.07.009

Cárdenas-arenas, A., Quindimil, A., DAVó-QUIñONERO, A., BAILóN-GARCíA, E., Lozano-CASTELLó, D., De-La-Torre, U., et al. (2020). Isotopic and *in situ* DRIFTS study of the CO2 methanation mechanism using Ni/CeO2 and Ni/Al2O3 catalysts. *Appl. Catal. B Environ.* 265, 118538. doi:10.1016/j.apcatb.2019.118538

Chen, P., Zhang, Y., Zhou, Y., and Dong, F. (2021). Photoelectrocatalytic carbon dioxide reduction: Fundamental, advances and challenges. *Nano Mater. Sci.* 3, 344–367. doi:10.1016/j.nanoms.2021.05.003

Coenen, K., Gallucci, F., Mezari, B., Hensen, E., and Van Sint Annaland, M. (2018). An *in-situ* IR study on the adsorption of CO2 and H2O on hydrotalcites. *J. CO2 Util.* 24, 228–239. doi:10.1016/j.jcou.2018.01.008

Deng, L. M., Hu, F., Ma, M. Y., Huang, S. C., Xiong, Y. X., Chen, H. Y., et al. (2021). Electronic modulation caused by interfacial Ni-O-M (M=Ru, Ir, Pd) bonding for accelerating hydrogen evolution kinetics. *Angew. Chem. Int. Ed. Engl.* 60, 22450–22456. doi:10.1002/ange.202110374

Deng, X. Y., Albero, J., Xu, L. Z., Garcia, H., and Li, Z. H. (2018). Construction of a stable Ru-Re hybrid system based on multifunctional MOF-253 for efficient photocatalytic CO2 reduction. *Inorg. Chem.* 57, 8276–8286. doi:10.1021/acs.inorgchem.8b00896

Feng, L., Wang, K. Y., Day, G. S., Ryder, M. R., and Zhou, H. C. (2020). Destruction of metal-organic frameworks: Positive and negative aspects of stability and lability. *Chem. Rev.* 120, 13087–13133. doi:10.1021/acs.chemrev.0c00722

Fernández-terán, R. J., and Sévery, L. (2021b). Coordination environment prevents access to intraligand charge-transfer states through remote substitution in rhenium(I) terpyridinedicarbonyl complexes. *Inorg. Chem.* 60, 1325–1333. doi:10.1021/acs.inorgchem.0c02914

Fernández-terán, R., and Sévery, L. (2021a). Living long and prosperous: Productive intraligand charge-transfer states from a rhenium(I) terpyridine photosensitizer with enhanced light absorption. *Inorg. Chem.* 60, 1334–1343. doi:10.1021/acs.inorgchem.0c01939

Fu, H.-C., You, F., Li, H.-R., and He, L.-N. (2019). CO2 capture and *in situ* catalytic transformation. *Front. Chem.* 7, 525. doi:10.3389/fchem.2019.00525

Gong, X., Tong, M., Brunetti, F. G., Seo, J., Sun, Y., Moses, D., et al. (2011). Bulk heterojunction solar cells with large open-circuit voltage: Electron transfer with small donor-acceptor energy offset. *Adv. Mat.* 23, 2272–2277. doi:10.1002/adma.201003768

He, X., and Wang, W.-N. (2018). MOF-Based ternary nanocomposites for better CO2photoreduction: Roles of heterojunctions and coordinatively unsaturated metal sites. *J. Mat. Chem. A Mat.* 6, 932–940. doi:10.1039/c7ta09192c

Jamjoum, H. A. A., Umar, K., Adnan, R., Razali, M. R., and Mohamad Ibrahim, M. N. (2021). Synthesis, characterization, and photocatalytic activities of graphene oxide/metal oxides nanocomposites: A review. *Front. Chem.* 9, 752276. doi:10.3389/fchem.2021.752276

Jiang, G., Peng, M., Hu, L., Ouyang, J., Lv, X., Yang, Z., et al. (2022). Electron-deficient Cuδ+ stabilized by interfacial Cu–O-Al bonding for accelerating electrocatalytic nitrate conversion. *Chem. Eng. J.* 435, 134853. doi:10.1016/j.cej.2022.134853

Karmakar, S., Barman, S., Rahimi, F. A., and Maji, T. K. (2021). Covalent grafting of molecular photosensitizer and catalyst on MOF-808: Effect of pore confinement toward visible light-driven CO2 reduction in water. *Energy Environ. Sci.* 14, 2429–2440. doi:10.1039/d0ee03643a

Li, X., Yu, J., Jaroniec, M., and Chen, X. (2019). Cocatalysts for selective photoreduction of CO2 into solar fuels. *Chem. Rev.* 119, 3962–4179. doi:10.1021/acs.chemrev.8b00400

Liu, H., Liu, Z., Yi, J., Ma, D., Xia, F., Tian, D., et al. (2021). A dual-signal electroluminescence aptasensor based on hollow Cu/Co-MOF-luminol and g-C3N4 for simultaneous detection of acetamiprid and malathion. *Sensors Actuators B Chem.*, 331, 129412. doi:10.1016/j.snb.2020.129412

Liu, L., Zhao, C., Miller, J. T., and Li, Y. (2017). Mechanistic study of CO2 photoreduction with H2O on Cu/TiO2 nanocomposites by *in situ* X-ray absorption and infrared spectroscopies. *J. Phys. Chem. C* 121, 490–499. doi:10.1021/acs.jpcc.6b10835

Ma, Z., Li, P., Ye, L., Zhou, Y., Su, F., Ding, C., et al. (2017). Oxygen vacancies induced exciton dissociation of flexible BiOCl nanosheets for effective photocatalytic CO2 conversion. *J. Mat. Chem. A Mat.* 5, 24995–25004. doi:10.1039/c7ta08766g

Singh, A. K., Jaiswal, N., Gautam, R. K., and Tiwari, I. (2021). Development of g-C3N4/Cu-DTO MOF nanocomposite based electrochemical sensor towards sensitive determination of an endocrine disruptor BPSIP. *J. Electroanal. Chem.* 887, 115170. doi:10.1016/j.jelechem.2021.115170

Sun, Y., Takacs, C. J., Cowan, S. R., Seo, J. H., Gong, X., Roy, A., et al. (2011). Efficient, air-stable bulk heterojunction polymer solar cells using MoOx as the anode interfacial layer. *Adv. Mat.* 23, 2226–2230. doi:10.1002/adma.201100038

Tang, J.-Y., Guo, R.-T., Pan, W.-G., Zhou, W.-G., and Huang, C.-Y. (2019). Visible light activated photocatalytic behaviour of Eu (III) modified g-C3N4 for CO2 reduction and H2 evolution. *Appl. Surf. Sci.* 467-468, 206–212. doi:10.1016/j.apsusc.2018.10.143

Wang, L., Jin, P., Huang, J., She, H., and Wang, Q. (2019a). Integration of copper(II)-Porphyrin zirconium metal–organic framework and titanium dioxide to construct Z-scheme system for highly improved photocatalytic CO2 reduction. *ACS Sustain. Chem. Eng.* 7, 15660–15670. doi:10.1021/acssuschemeng.9b03773

Wang, X.-K., Liu, J., Zhang, L., Dong, L.-Z., Li, S.-L., Kan, Y.-H., et al. (2019b). Monometallic catalytic models hosted in stable metal–organic frameworks for tunable CO2 photoreduction. *ACS Catal.* 9, 1726–1732. doi:10.1021/acscatal.8b04887

Xi, Y., Wei, W., Xu, Y., Huang, X., Zhang, F., and Hu, C. (2015). Coordination polymers based on substituted terpyridine ligands: Synthesis, structural diversity, and highly efficient and selective catalytic oxidation of benzylic C–H bonds. *Cryst. Growth & Des.* 15, 2695–2702. doi:10.1021/acs.cgd.5b00008

Xuan, X., Chen, S., Zhao, S., Yoon, J. Y., Boczkaj, G., and Sun, X. (2020). Carbon nanomaterials from metal-organic frameworks: A new material horizon for CO2 reduction. *Front. Chem.* 8, 573797. doi:10.3389/fchem.2020.573797

Yamazaki, Y., Onoda, T., Ishikawa, J., Furukawa, S., Tanaka, C., Utsugi, T., et al. (2019). Photocatalytic CO(2) reduction using various heteroleptic diimine-diphosphine Cu(I) complexes as photosensitizers. *Front. Chem.* 7, 288. doi:10.3389/fchem.2019.00288

Zha, Q. Q., Li, M. X., Liu, Z. H., and Ni, Y. H. (2020). Hierarchical Co, Fe-MOF-74/Co/carbon cloth hybrid electrode: Simple construction and enhanced catalytic performance in full water splitting. *ACS Sustain. Chem. Eng.* 8, 12025–12035. doi:10.1021/acssuschemeng.0c02993

Zhang, D., Han, X., Dong, T., Guo, X., Song, C., and Zhao, Z. (2018). Promoting effect of cyano groups attached on g-C3N4 nanosheets towards molecular oxygen activation for visible light-driven aerobic coupling of amines to imines. *J. Catal.* 366, 237–244. doi:10.1016/j.jcat.2018.08.018

Zhang, T., and Lin, W. B. (2014). Metal-organic frameworks for artificial photosynthesis and photocatalysis. *Chem. Soc. Rev.* 43, 5982–5993. doi:10.1039/c4cs00103f

Zhao, J., Wang, T., Deng, J., Shu, C.-M., Zeng, Q., Guo, T., et al. (2020a). Microcharacteristic analysis of CH4 emissions under different conditions during coal spontaneous combustion with high-temperature oxidation and *in situ* FTIR. *Energy* 209, 118494. doi:10.1016/j.energy.2020.118494

Zhao, Y., Shi, T., Shang, J., Ding, L., Cao, X., Chen, C., et al. (2020b). Rapid proton exchange between surface bridging hydroxyls and adsorbed molecules on TiO2, *Appl. Catal. B Environ.*, 277. 119234, doi:10.1016/j.apcatb.2020.119234

Zheng, L., Zhu, T., Xu, W., Liu, L., Zheng, J., Gong, X., et al. (2018). Solution-processed broadband polymer photodetectors with a spectral response of up to 2.5 μm by a low bandgap donor–acceptor conjugated copolymer. *J. Mat. Chem. C Mat.* 6, 3634–3641. doi:10.1039/c8tc00437d

Zhu, Q., Cao, Y., Tao, Y., Li, T., Zhang, Y., Shang, H., et al. (2021). CO2 reduction to formic acid via NH2-C@Cu2O photocatalyst *in situ* derived from amino modified Cu-MOF. *J. CO2 Util.*, 54, 101781. doi:10.1016/j.jcou.2021.101781